RESEARCH ARTICLE

Conical Intersection versus Avoided Crossing: Geometric Phase Effect in Molecular High-Order Harmonics

Guanglu Yuan[1,2], **Ruifeng Lu**[1]*, **Shicheng Jiang**[2]*, and **Konstantin Dorfman**[2,3,4,5]*

[1]Institute of Ultrafast Optical Physics, MIIT Key Laboratory of Semiconductor Microstructure and Quantum Sensing, Department of Applied Physics, Nanjing University of Science and Technology, Nanjing 210094, China. [2]State Key Laboratory of Precision Spectroscopy, East China Normal University, Shanghai 200062, China. [3]Center for Theoretical Physics and School of Science, Hainan University, Haikou 570228, China. [4]Collaborative Innovation Center of Extreme Optics, Shanxi University, Taiyuan, Shanxi 030006, China. [5]Himalayan Institute for Advanced Study, Unit of Gopinath Seva Foundation, MIG 38, Avas Vikas, Rishikesh, Uttarakhand 249201, India.

*Address correspondence to: rflu@njust.edu.cn (R.L.); scjiang@lps.ecnu.edu.cn (S.J.); dorfmank@hainanu.edu.cn (K.D.)

Nonadiabatic dynamics around an avoided crossing or a conical intersection play a crucial role in the photoinduced processes of most polyatomic molecules. The present work shows that the topological phase in conical intersection makes the behavior of pump-probe high-order harmonic signals different from the case of avoided crossing. The coherence built up when the system crosses the avoided crossing will lead to the oscillatory behavior of the spectrum, while the geometric phase erodes these oscillations in the case of conical intersection. Additionally, the dynamical blueshift and the splitting of the time-resolved spectrum allow capturing the snapshot dynamics with the sub-femtosecond resolution.

Introduction

The avoided crossing (AC) and conical intersection (CI) in polyatomic molecules play important roles in various photophysical and photochemical dynamical processes [1,2]. Benefiting from the progress in laser technology, many optical methods have been developed to probe the ultrafast dynamics of molecules, especially the nonadiabatic dynamics in the vicinity of CI [3–10]. Attosecond transient-absorption spectroscopy succeeded in mapping the AC dynamics directly [11], and recently achieving the sub-7-fs resolution in CI by extending the attosecond pulse to carbon K-edge [3]. A background-free technique called TRUECARS (Transient Redistribution of Ultrafast Electronic Coherences in Attosecond Raman Signals) [12–14] was proposed to detect the electronic coherence generated by the CI. In the past decades, high-harmonic spectroscopy the (HHS) has matured into a powerful approach to study the structure and dynamics of molecules [15–23]. For example, Wörner et al. [24,25] reported the application of HHS to detect CI dynamics.

While both CI and AC can induce a nonradiative transition, most of the previous works did not provide a specific recipe for discriminating between the CI and the AC. The main topological feature of CI that distinguishes it from the AC is that the wavepacket accumulates the geometric phase (GP) as it propagates around the CI. In 1963, Herzberg and Longuet-Higgins [26] showed that the electronic wave function changes its sign for any closed path in the nuclear parameter space that encircles a CI. Later, in 1984, Berry pointed that this sign change is a special case of a more general GP factor [27], often referred to as a "Berry Phase". Further applications of GP include the hydrogen exchange reaction [28,29] and the dissociation spectrum [30–33]. Since the high-harmonic generation (HHG) is driven by the ultrashort laser fields, and the HHS is particularly sensitive to the variation of ionization potential along with the population and the coherence between the superposed states [34], the HHS is an ideal tool to simultaneously monitor the ultrafast dynamics around the CI or the AC and to identify GP effect.

Methods

In this study, we apply the pump-probe HHS driven by a few-cycle infrared (IR) pulse to distinguish the CI from the AC. Figure 1A shows a schematic of the pump-probe process where the wavepacket initially located on the ground state S_0 is excited to state S_1 by an ultrafast vacuum ultraviolet (VUV) pulse. The nuclear wavepacket then dissociates along 2 branches encircling the CI or AC as indicated by the white arrows in Fig. 1A. Meanwhile, a part of the wavepacket passes through the CI or AC. Finally, a delayed strong IR probe laser is sent to generate

HHS. To model the pump-probe HHG dynamics, the time-dependent Schrödinger equation (TDSE) in the diabatic representation (see Supplementary Materials for details) is solved (atomic units are used unless otherwise indicated):

$$i\frac{\partial}{\partial t}\begin{pmatrix} \chi_0(\vec{R},t) \\ \chi_1(\vec{R},t) \\ \chi_2(\vec{R},t) \\ \chi_C(\vec{R},\vec{k},t) \end{pmatrix} = \left(\hat{T} + \hat{H}_{el}\right)\begin{pmatrix} \chi_0(\vec{R},t) \\ \chi_1(\vec{R},t) \\ \chi_2(\vec{R},t) \\ \chi_C(\vec{R},\vec{k},t) \end{pmatrix}, \quad (1)$$

with Hamiltonian $\hat{H}_{el}$ defined as follows:

$$\begin{bmatrix} V_0(\vec{R}) & \vec{d}_{01}\cdot\vec{E}(t) & 0 & 0 \\ \vec{d}_{01}^*\cdot\vec{E}(t) & V_1(\vec{R}) & V_{12}(\vec{R}) & D_{1C}(\vec{R},\vec{k},t) \\ 0 & V_{12}^*(\vec{R}) & V_2(\vec{R}) & D_{2C}(\vec{R},\vec{k},t) \\ 0 & D_{1C}^*(\vec{R},\vec{k},t) & D_{2C}^*(\vec{R},\vec{k},t) & \tilde{V}_C(\vec{R},\vec{k},t) \end{bmatrix}. \quad (2)$$

Here, $\hat{T}$ is the nuclear kinetic energy operator and $\vec{E}(t)$ is the electric field. χ_n is the nuclear wave function moving on state S_n. V_n and V_C represent the potential energy surfaces (PESs) for the neutral bound states S_n and the ionic ground state S_C, respectively. In the following simulation, the V_C is assumed to be the same as V_1, except a vertical energy difference. $\tilde{V}_C(\vec{R},\vec{k},t) = V_C(\vec{R}) + (\vec{k}+\vec{A}(t))^2/2$ is the equivalent PESs of continuum state S_C, with the vector potential $\vec{A}(t)$ and the electronic momentum $\vec{k}$. $D_{nC}(\vec{R},\vec{k},t) = \vec{E}(t)\cdot\vec{d}_{nC}(\vec{R},\vec{k}+\vec{A}(t))$ is the product of the laser field $\vec{E}(t)$ and the transition dipole moments (TDMs) $\vec{d}_{nC}$ between the states S_n and S_C. $\vec{d}_{nC}$ at each $\vec{R}$ takes the form of the TDMs for the hydrogen-like atoms [35]. $\vec{d}_{01}$

is a constant TDM between the states S_0 and S_1. V_{12} is the non-adiabatic coupling (NAC) term between S_1 and S_2, and is related to the mixing angle $\theta = 0.5\arctan(2V_{12}/(V_1-V_2))$ [36].

Here, $\Delta\theta$ is used to represent the difference between the mixing angles of the beginning and ending positions of a path. In the CI case, V_{12} is anti-symmetric with respect to the mirror plane. Encircling the CI point with a closed loop C, $\Delta\theta$ evolves from 0 to π or $-\pi$ [37]. Since the Berry phase $\gamma = \oint_C \nabla\theta\cdot d\vec{s}$ [38–40], this phase shift of π is considered as an accumulation of GP. For the system with AC, the NAC term $V_{12}' = |V_{12}| + \xi$ (ξ is an arbitrarily small constant) is symmetric with respect to $R_2 = 0$. Assuming the same encirclement as before, $\Delta\theta$ changes from 0 to $\pi/2$ or $-\pi/2$ and back to 0, resulting in zero GP accumulation. (See Fig. S1 for a detailed analysis of the $\Delta\theta$ and associated GP in both cases.) Therefore, the GP effect has been included with the anti-symmetric V_{12} and has been excluded if we set $V_{12}' = |V_{12}|$ [41], as shown in Fig. 2C. The variation of $\Delta\theta$ along 2 semicircles in the clockwise and the counter-clockwise directions around CI or AC is labeled respectively in Fig. 2C, as these 2 semicircles are similar to the trajectories of nuclear wavepackets. Obviously, the difference in symmetry of the NAC term leads to different changes in $\Delta\theta$ along the 2 semicircular paths, reflecting the difference of GP in the 2 cases.

The polarization can be recast as

$$\vec{P}(t) = \iint d\vec{R}\,d\vec{k}\left[\chi_1(\vec{R},t)\chi_C^*(\vec{R},\vec{k},t)\vec{d}_{1C}(\vec{R},\vec{k}+\vec{A}(t))+ \chi_2(\vec{R},t)\chi_C^*(\vec{R},\vec{k},t)\vec{d}_{2C}(\vec{R},\vec{k}+\vec{A}(t))\right]+c.c.$$

(3)

after propagating the TDSE by the split operator algorithm based on fast Fourier transform. Finally, the HHS can be obtained by the Fourier transformation of $\vec{P}(t)$

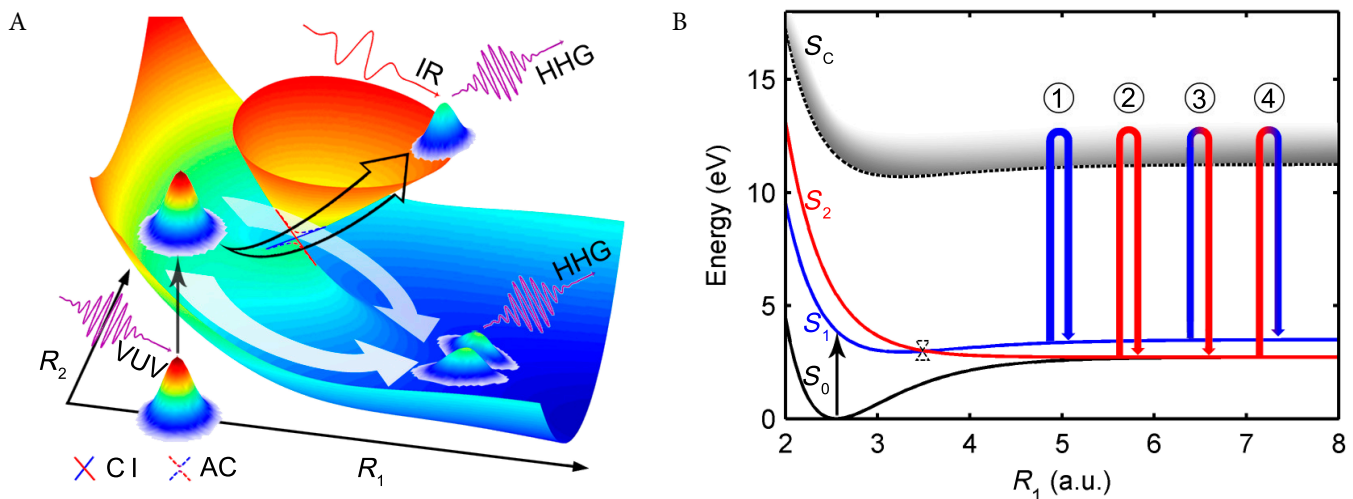$$I(\omega) \propto \omega^4\left|\int_{-\infty}^{\infty}\vec{P}(t)e^{i\omega t}dt\right|^2. \quad (4)$$

Fig. 1. (A) The adiabatic PESs and a schematic diagram of the pump-probe process. The wavepacket is the pumped to the excited state S_1 by the VUV pulse. Then, a part of it passes through the CI (AC) (shown by the black hollow arrow), and the rest is divided into 2 parts bypassing the CI (AC) in the clockwise and the counterclockwise directions (shown by the white translucent arrow). Finally, the HHG of the excited molecule is obtained with a time-delayed IR pulse. (B) 1D slices of the diabatic PESs at $R_2 = 0$. The dashed funnel indicates the location of the CI (AC). The arrows marked by ①, ②, ③, and ④ correspond to the 4 different channels in the HHG process.
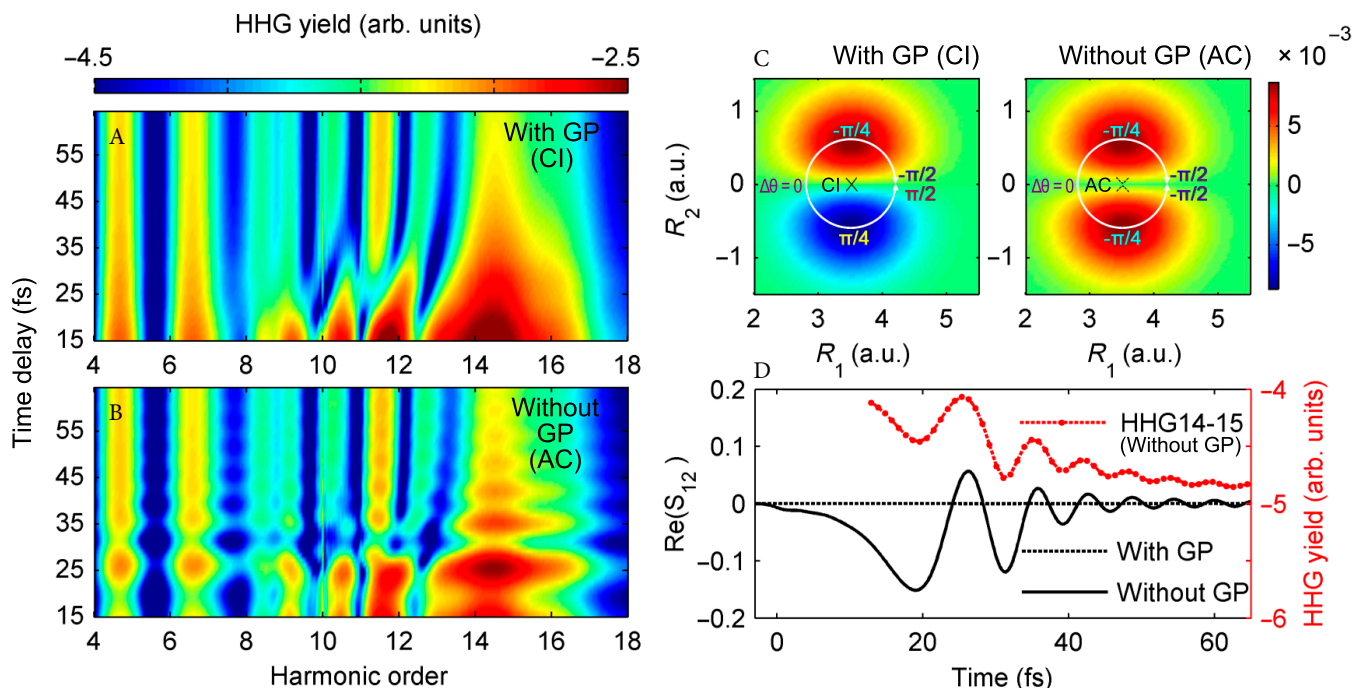
Fig. 2. The HHS as a function of time delay (A) with and (B) without GP in the logarithmic scale. The peak of the VUV pulse is set as the time origin. Time delay corresponds to the interval between the peak of the IR and the origin. Harmonic order is taken relative to the IR single photon energy. (C) 2D plots for the NAC element V_{12} (with GP) and V'_{12} (without GP). The position of CI and AC and the variation of mixing angle θ along the white solid line with arrows are marked. (D) Real part of the time-dependent overlap integral S_{12} with (black dotted line) and without (black solid line) GP in the absence of IR laser. The intensity of delay-dependent harmonics (red dotted line) is obtained by integrating harmonics between the 14th and 15th order in (B).

The parameters of the diabatic molecular model based on multiple 2-dimensional (2D) PESs are shown in the Supplementary Materials. We employ the VUV pulse with the laser parameters of wavelength $\lambda_1 = 318$ nm, peak intensity $I_1 = 10^{13}$ W/cm^2, and full width at half maximum (FWHM) $\tau_1 = 3.18$ fs, which can pump about 70% of the electron population from the ground state S_0 to the excited state S_1. Regarding the delayed IR pulse, the parameters are wavelength $\lambda_2 = 1{,}600$ nm, intensity $I_2 = 10^{13}$ W/cm^2, and FWHM $\tau_2 = 5.33$ fs. Both IR and VUV pulses have a Gaussian envelope. The initial momentum of the ionized electron is set to $\vec{k}_0 = 0$ instead of integrating over the entire range of momentum. The contribution of the ground state to the HHG has been neglected. The delay-dependent HHS is shown in Fig. 2A (includes the GP) and Fig. 2B (excludes the GP), in which the latter shows strong oscillations, while the former does not.

Results and Discussion

As the wavepacket passes through the CI or AC, electronic coherence can be built up and the system is excited with the both populations ρ_{S_1}, ρ_{S_2}, and coherences $\rho_{S_1S_2}$, $\rho_{S_2S_1}$ before the IR arrives. Due to the slow motion relative to the ultrafast IR pulse, the nucleus can be treated in the frozen-nuclear approximation (FNA) in the HHG process. In the FNA and the strong-field approximation (SFA) [35], the electronic polarization for the fixed nuclear coordinate $\vec{R}_0$ and the time delay τ can be written as:

$$\vec{P}'\left(t, \tau; \vec{R}_0\right) = \sum_{m,n=1}^{2} \vec{P}'_{mn}\left(t, \tau; \vec{R}_0\right), \tag{5}$$

where $\vec{P}'_{mn}$ are the contributions from different channels:

$$\vec{P}'_{mn}\left(t, \tau; \vec{R}_0\right) = \int d\vec{k} \int_{\tau}^{t} dt' i\vec{E}\left(t'\right) \alpha_{mn}\left(t, \tau; \vec{R}_0\right)$$
$$\times \vec{d}^*_{mC}\left(\vec{k} + \vec{A}(t); \vec{R}_0\right) \vec{d}_{nC}\left(\vec{k} + \vec{A}(t'); \vec{R}_0\right) \tag{6}$$
$$\times e^{-i\int_{t'}^{t}\left(\left(\vec{k}+\vec{A}(t'')\right)^2/2 + V_C\left(\vec{R}_0\right) - V_n\left(\vec{R}_0\right)\right)dt''} + c.c.,$$

with

$$\alpha_{mn}\left(t, \tau; \vec{R}_0\right) =$$
$$\chi^*_m\left(\tau; \vec{R}_0\right)\chi_n\left(\tau; \vec{R}_0\right) e^{i\left(V_m\left(\vec{R}_0\right) - V_n\left(\vec{R}_0\right)\right)(t-2\tau)}. \tag{7}$$

χ_m and χ_n are not dependent on the ionization time t' and the recombination time t since the depletion of the excited states can be neglected [35]. Equation 6 is similar to the traditional SFA model except that it is weighted by α_{mn}. As indicated in Fig. 1B, $\vec{P}'_{11}$, $\vec{P}'_{22}$, $\vec{P}'_{21}$, and $\vec{P}'_{12}$ correspond to the channels ①, ②, ③, and ④, respectively. We can classify the HHG process into the direct (① and ②) and the indirect (③ and ④) ionization-recombination channels. The initial and the final states of a direct (indirect) channel where the electron is ionized and recombined are the same (different). Ignoring the phase term and integrating Eq. 7 over $\vec{R}$, the overlap integral $S_{mn} = \int_{\vec{R}} d\vec{R}\, \chi^*_m\left(t; \vec{R}\right)\chi_n\left(t; \vec{R}\right)$ is obtained. Previously, many works used the overlap integral S_{mn} to probe the nuclear dynamics with the sub-cycle resolution [12,42,43]. According to Eq. 7, unlike the direct channels related to the populations ρ_{S_1} and ρ_{S_2}, the indirect ones, e.g., $n \neq m$, yield an off-diagonal coherence, which results in the oscillating behavior with respect to the interpulse delay.
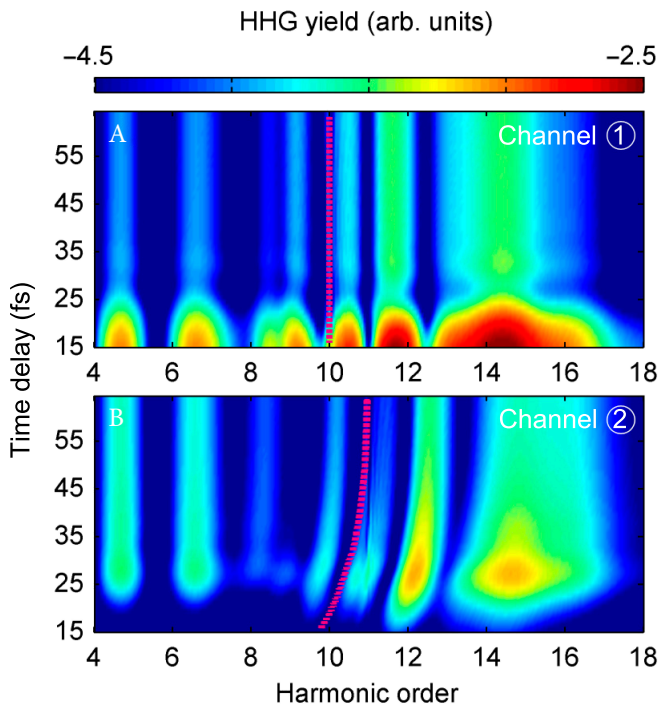
Fig. 3. Time-resolved HHS generated by (A) channel ① and (B) channel ② with GP. The 2 time-varying energy difference $V_C - V_1$ and $V_C - V_2$ is plotted in (A) and (B) depicted by the dashed purple line. These are calculated at the coordinates of the 2 excited state wavepacket maximum positions, respectively.
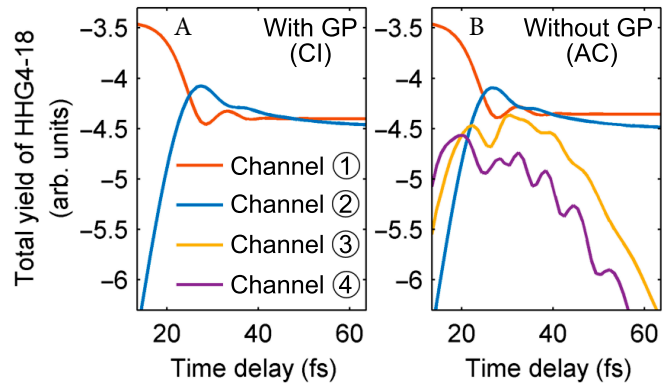

Fig. 4. Time-resolved HHS from the 4 channels (① to ④) obtained after integrating Eq. 6 over $\vec{R}$ and integrating the harmonics in the 4th- to 18th-order range. The total yield is plotted in logarithmic scale. (A) and (B) correspond to the results with and without GP effect, respectively. With the GP effect, the harmonic yields of channels ③ and ④ are around −19 orders of magnitude, and are thus omitted in (A).

We next discuss the eroding of oscillations in the CI case. The symmetric wavepackets in state S_1 will be changed to the anti-symmetric in state S_2 when it is transferred by the anti-symmetric NAC term V_{12}. Once the integral of the polarization (Eq. 6) is calculated over the whole nuclear space, the contribution from the indirect channel will vanish. That is the reason that the oscillation feature disappears in HHS for the case of CI. This conclusion can be proved by Fig. 2D, where the real part of S_{12} with and without GP is plotted together with the time delay-dependent HHS intensity.

Another important phenomenon is that in both Fig. 2A and B, the delay-dependent peaks of the spectrum split. Obviously, this phenomenon is not related to the GP effect and originates rather from the direct channels because the indirect channels vanish in the CI case as explained above. Thus, the total harmonics in Fig. 2A can be well divided into channels ① and ②, by choosing one particular term in the square brackets of Eq. 3 instead of summing the 2 terms, as shown in Fig. 3. As a result, the time-resolved HHS from the channel ② shows the blueshift while the contribution from the channel ① does not. According to Eq. 6, the total phase of the qth-order harmonic generated from channel ① or channel ② can be written as [44,45]

$$\phi_q(t) = q\omega_{IR}t$$

$$+ \int_{t'}^{t} \left(\left(\vec{k} + \vec{A}(t'')\right)^2/2 + V_C\left(\vec{R}_0\right) - V_n\left(\vec{R}_0\right) \right) dt'', \quad (8)$$

with ω_{IR} as the central frequency of IR laser. Therefore, the instantaneous frequency of each harmonic is given by

$$\omega_q(t) = \frac{\partial \phi_q(t)}{\partial t}$$

$$= q\omega_{IR} + \left(\vec{k} + \vec{A}(t)\right)^2/2 + \left(V_C\left(\vec{R}_0\right) - V_n\left(\vec{R}_0\right)\right). \quad (9)$$

Here, the first and the second terms in the right-hand side (RHS) depend solely on the driving laser field, which does not depend on the interpulse time delay. Thus, the blueshift originates from the third term in the RHS of Eq. 9, e.g., the energy difference between the ionic ground state S_C and the state S_n from where the electron ionizes. In Fig. 3A and B, the dashed purple lines are the delay-dependent energy differences for $V_C - V_1$ and $V_C - V_2$ at the nuclear coordinates corresponding to the maximum of the delay-dependent wavepackets. It is apparent that the energy differences are consistent with the blueshifts. The 2 paths result in the split of the total HHS in Fig. 2A and B, which clearly indicates that the nuclear wavepacket passes through the CI or the AC at the corresponding time delay of 20 to 30 fs.

Frequency modulation of HHS has been widely investigated previously, as summarized in Ref. [46]. Once the HHS originated from the leading (falling) edge of the laser envelop dominates, the final signal shows the blueshift (redshift). In our case, since the FNA is adopted, the modulation of the ionization potential at the pulse duration timescale can be neglected. The frequency modulation contributed by the leading and falling edges can be neglected in the present work. In fact, the present blueshift can be observed only in the case of few-cycle lasers. Thus, the time resolution of the present blueshift is determined by the FWHM of the driving laser.

Figure 4 depicts the time-resolved integrated intensity for the HHS from the 4 channels, which is calculated using Eq. 6 and obtained by integrating over $\vec{R}$ and energy (see Fig. S2 for HHS before integrating in the energy range). It indicates that the direct channels also show weak oscillations, which are proportional to the populations of the excited states. These results are in full agreement with those obtained in Ref. [24], in which the oscillation feature originating from the population dynamics has been observed by the transient grating technique. The contributions of the indirect channels are proportional to the

coherence of the 2 excited states and thus show much stronger oscillations.

Conclusion

We show that the time-resolved HHS can probe the topological phase in CI and distinguish its quantitative behavior from the case of AC. When the nuclear wavepacket passes through the CI and AC, electronic coherence may emerge as a consequence of NAC. The electronic coherence leads to the oscillatory feature in the HHS in the case of AC, while the vanishing oscillations in the case of CI are consequences of the symmetry breaking caused by the GP. Additionally, the HHS indicates the splitting of the signal into 2 peaks as the nuclear wavepacket passes through the CI or AC, which is attributed to the different frequency shifts of the HHS contributed by the different direct channels. The combined effects of the peak splitting along the dynamical blueshift indicate a possibility to capture the real-time nonadiabatic molecular dynamics with the sub-femtosecond time resolution. Our result will benefit substantially from the ability to separately track electronic coherences and populations. A near-future development of the multi-dimensional HHS [47,48] could be a potential tool to improve these results and track the dynamics of CI or AC with even higher resolution. Although our 2D model simulations shed valuable light on the GP effect in pump-probe HHS of molecules, the present methodology can be further developed for the real polyatomic molecules with higher dimensionalities. It should be noted that defining a high-dimensional path encircling the CI point in a real system is not an easy task. Nevertheless, the adequate models of describing the dynamics of the wavepacket passing through the seam-like CI [13] have been constructed, making it a promising approach that can be utilized in high-harmonic regime as well.

Data Availability

The data that support the plots within this paper will be available from the corresponding authors upon reasonable request.

Supplementary Materials

The time-dependent Schrödinger equation of a laser-driven molecule with conical intersection and the parameters for the 2D model based on multiple potential energy surfaces in the diabatic representation.

Fig. S1. The variation of the mixing angle along a closed path encircling the conical intersection or the avoided crossing.
Fig. S2. The delay-dependent high harmonic spectroscopy from different ionization-recombination channels.

References

1. Domcke W, Yarkony DR. Role of conical intersections in molecular spectroscopy and photoinduced chemical dynamics. *Annu Rev Phys Chem*. 2012;63(1):325–352.
2. Worth GA, Cederbaum LS. Beyond Born-Oppenheimer: Molecular dynamics through a conical intersection. *Annu Rev Phys Chem*. 2004;55(1):127–158.
3. Zinchenko KS, Ardana-Lamas F, Seidu I, Neville SP, van der Veen J, Lanfaloni VU, Schuurman MS, Wörner HJ. Sub-7-femtosecond conical-intersection dynamics probed at the carbon K-edge. *Science*. 2021;371(6528):489–494.
4. Hosseinizadeh A, Breckwoldt N, Fung R, Sepehr R, Schmidt M, Schwander P, Santra R, Ourmazd A. Few-fs resolution of a photoactive protein traversing a conical intersection. *Nature*. 2021;599(7886):697–701.
5. Nam Y, Keefer D, Nenov A, Conti I, Aleotti F, Segatta F, Lee JY, Garavelli M, Mukamel S. Conical intersection passages of molecules probed by X-ray diffraction and stimulated Raman spectroscopy. *J Phys Chem Lett*. 2021;12(51):12300–12309.
6. Timmers H, Zhu X, Li Z, Kobayashi Y, Sabbar M, Hollstein M, Reduzzi M, Martínez TJ, Neumark DM, Leone SR. Disentangling conical intersection and coherent molecular dynamics in methyl bromide with attosecond transient absorption spectroscopy. *Nat Commun*. 2019;10:3133.
7. Neville SP, Chergui M, Stolow A, Schuurman MS. Ultrafast X-ray spectroscopy of conical intersections. *Phys Rev Lett*. 2018;120(24):243001.
8. Kowalewski M, Fingerhut BP, Dorfman KE, Bennett K, Mukamel S. Simulating coherent multidimensional spectroscopy of nonadiabatic molecular processes: From the infrared to the X-ray regime. *Chem Rev*. 2017;117(19): 12165–12226.
9. Pan S, Hu C, Zhang Z, Lu P, Lu C, Zhou L, Wang J, Sun F, Qiang J, Li H, et al. Low-energy protons in strong-field dissociation of H_2^+ via dipole-transitions at large bond lengths. *Ultrafast Sci*. 2022;2022:9863548.
10. Guo Z, Ge P, Fang Y, Dou Y, Yu X, Wang J, Gong Q, Liu Y. Probing molecular frame Wigner time delay and electron wavepacket phase structure of CO molecule. *Ultrafast Sci*. 2022;2022:9802917.
11. Kobayashi Y, Chang KF, Zeng T, Neumark DM, Leone SR. Direct mapping of curve-crossing dynamics in IBr by attosecond transient absorption spectroscopy. *Science*. 2019;365(6448):79–83.
12. Kowalewski M, Bennett K, Dorfman KE, Mukamel S. Catching conical intersections in the act: Monitoring transient electronic coherences by attosecond stimulated X-ray Raman signals. *Phys Rev Lett*. 2015;115:193003.
13. Keefer D, Schnappinger T, de Vivie-Riedle R, Mukamel S. Visualizing conical intersection passages via vibronic coherence maps generated by stimulated ultrafast X-ray Raman signals. *Proc Natl Acad Sci USA*. 2020;117(39): 24069–24075.
14. Keefer D, Mukamel S. Selective enhancement of spectroscopic features by quantum optimal control. *Phys Rev Lett*. 2021;126:163202.

15. Kanai T, Minemoto S, Sakai H. Quantum interference during high-order harmonic generation from aligned molecules. *Nature*. 2005;435(7041):470–474.

16. Mairesse Y, Higuet J, Dudovich N, Shafir D, Fabre B, Mével E, Constant E, Patchkovskii S, Walters Z, Ivanov MY, et al. High harmonic spectroscopy of multichannel dynamics in strong-field ionization. *Phys Rev Lett*. 2010;104:213601.

17. Vozzi C, Negro M, Calegari F, Sansone G, Nisoli M, de Silvestri S, Stagira S. Generalized molecular orbital tomography. *Nat Phys*. 2011;7(10):822–826.

18. Frumker E, Kajumba N, Bertrand JB, Wörner HJ, Hebeisen CT, Hockett P, Spanner M, Patchkovskii S, Paulus GG, Villeneuve DM, et al. Probing polar molecules with high harmonic spectroscopy. *Phys Rev Lett*. 2012;109:233904.

19. Wong MCH, Le AT, Alharbi AF, Boguslavskiy AE, Lucchese RR, Brichta JP, Lin CD, Bhardwaj VR. High harmonic spectroscopy of the cooper minimum in molecules. *Phys Rev Lett*. 2013;110:033006.

20. Baykusheva D, Ahsan MS, Lin N, Wörner HJ. Bicircular high-harmonic spectroscopy reveals dynamical symmetries of atoms and molecules. *Phys Rev Lett*. 2016;116:123001.

21. Suárez N, Chacón A, Pérez-Hernández JA, Biegert J, Lewenstein M, Ciappina MF. High-order-harmonic generation in atomic and molecular systems. *Phys Rev A*. 2017;95:033415.

22. Uzan AJ, Soifer H, Pedatzur O, Clergerie A, Larroque S, Bruner BD, Pons B, Ivanov M, Smirnova O, Dudovich N. Spatial molecular interferometry via multidimensional high-harmonic spectroscopy. *Nat Photonics*. 2020;14(3):188–194.

23. Peng P, Marceau C, Villeneuve DM. Attosecond imaging of molecules using high harmonic spectroscopy. *Nat Rev Phys*. 2019;1(2):144–155.

24. Wörner HJ, Bertrand JB, Fabre B, Higuet J, Ruf H, Dubrouil A, Patchkovskii S, Spanner M, Mairesse Y, Blanchet V, et al. Conical intersection dynamics in NO_2 probed by homodyne high-harmonic spectroscopy. *Science*. 2011;334(6053):208–212.

25. Kraus PM, Arasaki Y, Bertrand JB, Patchkovskii S, Corkum PB, Villeneuve DM, Takatsuka K, Wörner HJ. Time-resolved high-harmonic spectroscopy of nonadiabatic dynamics in NO_2. *Phys Rev A*. 2012;85:043409.

26. Herzberg G, Longuet-Higgins HC. Intersection of potential energy surfaces in polyatomic molecules. *Discuss Faraday Soc*. 1963;35:77–82.

27. Berry MV. Quantal phase factors accompanying adiabatic changes. *Proc R Soc Lond A Math Phys Sci*. 1984;392(1802):45–57.

28. Juanes-Marcos JC, Althorpe SC, Wrede E. Theoretical study of geometric phase effects in the hydrogen-exchange reaction. *Science*. 2005;309(5738):1227–1230.

29. Yuan D, Guan Y, Chen W, Zhao H, Yu S, Luo C, Tan Y, Xie T, Wang X, Sun Z, et al. Observation of the geometric phase effect in the H + HD $\rightarrow$ H_2 + D reaction. *Science*. 2018;362(6420):1289–1293.

30. Abe M, Ohtsuki Y, Fujimura Y, Lan Z, Domcke W. Geometric phase effects in the coherent control of the branching ratio of photodissociation products of phenol. *J Chem Phys*. 2006;124(22):224316.

31. Nix M, Devine A, Dixon R, Ashfold M. Observation of geometric phase effect induced photodissociation dynamics in phenol. *Chem Phys Lett*. 2008;463(4–6):305–308.

32. Bouakline F. Investigation of geometric phase effects in photodissociation dynamics at a conical intersection. *Chem Phys*. 2014;442:31–40.

33. Xie C, Malbon CL, Yarkony DR, Xie D, Guo H. Signatures of a conical intersection in adiabatic dissociation on the ground electronic state. *J Am Chem Soc*. 2018;140(6):1986–1989.

34. Kraus PM, Zhang SB, Gijsbertsen A, Lucchese RR, Rohringer N, Wörner HJ. High-harmonic probing of electronic coherence in dynamically aligned molecules. *Phys Rev Lett*. 2013;111:243005.

35. Lewenstein M, Balcou P, Ivanov MY, L'Huillier A, Corkum PB. Theory of high-harmonic generation by low-frequency laser fields. *Phys Rev A*. 1994;49:2117–2132.

36. Xie C, Yarkony DR, Guo H. Nonadiabatic tunneling via conical intersections and the role of the geometric phase. *Phys Rev A*. 2017;95:022104.

37. Ryabinkin IG, Joubert-Doriol L, Izmaylov AF. Geometric phase effects in nonadiabatic dynamics near conical intersections. *Acc Chem Res*. 2017;50(7):1785–1793.

38. Farag MH, Mandal A, Huo P. Polariton induced conical intersection and berry phase. *Phys Chem Chem Phys*. 2021;23:16868–16879.

39. Baer M. Nonadiabatic effects in molecular adiabatic systems: Application to linear plus quadratic E⊗e system. *J Chem Phys*. 1997;107(24):10662–10666.

40. Baer M. *Beyond born–Oppenheimer*. Hoboken (NJ): John Wiley & Sons, Ltd; 2006. Chapter 3, Model studies; p. 58–83.

41. Schüppel F, Schnappinger T, Bäuml L, de Vivie-Riedle R. Waveform control of molecular dynamics close to a conical intersection. *J Chem Phys*. 2020;153:224307.

42. Baker S, Robinson JS, Haworth CA, Teng H, Smith RA, Chirila CC, Lein M, Tisch JW, Marangos JP. Probing proton dynamics in molecules on an attosecond time scale. *Science*. 2006;312(5772):424–427.

43. Le A-T, Morishita T, Lucchese RR, Lin CD. Theory of high harmonic generation for probing time-resolved large-amplitude molecular vibrations with ultrashort intense lasers. *Phys Rev Lett*. 2012;109:203004.

44. Chang Z, Rundquist A, Wang H, Christov I, Kapteyn HC, Murnane MM. Temporal phase control of soft-x-ray harmonic emission. *Phys Rev A*. 1998;58:R30–R33.

45. Shin HJ, Lee DG, Cha YH, Hong KH, Nam CH. Generation of nonadiabatic blueshift of high harmonics in an intense femtosecond laser field. *Phys Rev Lett*. 1999;83:2544–2547.

46. Bian X-B, Bandrauk AD. Probing nuclear motion by frequency modulation of molecular high-order harmonic generation. *Phys Rev Lett*. 2014;113:193901.

47. Jiang S, Dorfman K. Detecting electronic coherences by time-domain high-harmonic spectroscopy. *Proc Natl Acad Sci USA*. 2020;117(18):9776–9781.

48. Jiang S, Kowalewski M, Dorfman KE. Multi-wave mixing in the high harmonic regime: Monitoring electronic dynamics. *Opt Express*. 2021;29(4):4746–4754.